PHYSICAL REVIEW B **80**, 174419 (2009)

Mechanism of exchange bias for isolated nanoparticles embedded in an antiferromagnetic matrix

Valera P. Shcherbakov
Geophysical Observatory "Borok," Yaroslavskaja Oblast 151742, Russia

Karl Fabian* and Suzanne A. McEnroe
Geological Survey of Norway, Leiv Eirikssons vei 39, N-7491 Trondheim, Norway

(Received 6 January 2009; revised manuscript received 29 September 2009; published 20 November 2009)

Single magnetic nanodots, exchange coupled to an antiferromagnetic (AF) matrix, can produce large exchange bias, while superparamagnetic behavior of the nanodots is suppressed. The exchange bias originates from the formation of a (quasi)spherical domain wall inside the AF matrix when the particle moment rotates under the influence of an external magnetic field. Micromagnetic calculations show that for isolated nanodots the energy of this domain wall increases nearly quadratically with the deflection angle of the nanodot moment. By introducing the corresponding quadratic energy term in a modified Stoner-Wohlfarth model, a two-parameter family of hysteresis loops is obtained, depending on scaled anisotropy energy and field direction. The loops are represented in a phase diagram with three main regions, containing (1) reversible loops, (2) irreversible loops with a metastable 180° AF domain wall, and (3) loops with metastable AF domain walls with 360° or higher rotation angles. According to this model, isolated nanodots display reversible negatively biased loops for all field directions, if their anisotropy energy is small in comparison to the AF domain-wall energy. For higher anisotropy, irreversible, mostly negatively biased, loops result from switching between the ground state and an higher-energy inverse state with a 180° AF domain wall. At even higher anisotropy energy, the loops can show positive exchange bias after an initial "training branch." Switching after "training" takes place between states having a 180° and a 360° AF domain wall, respectively. While for thin films, the bias field increases in inverse proportion to thickness, for nanodots it increases in inverse proportion to the square of particle diameter. Therefore, nanodots can show significantly larger exchange bias than thin films of similar dimension. Hysteresis loops, obtained from averaging over directions and sizes using the modified Stoner-Wohlfarth model, were compared to measurements from a natural sample with nanometer-scale ilmenite-exsolution lamellae in a hematite matrix. The shapes of the hysteresis difference, the difference between upper and lower branches, are similar for model and experiment, whereby increasing temperature in the measurement corresponds qualitatively to decreasing the relative anisotropy energy in the model.

DOI: 10.1103/PhysRevB.80.174419 PACS number(s): 75.60.Ch, 75.50.Tt, 75.60.Ej, 75.75.+a

I. INTRODUCTION

A. Exchange bias in coupled systems

Exchange bias has been found in thin films and nanoparticle structures, containing exchange-coupled interfaces between two different magnetic materials.[1,2] Typical examples are thin films containing ferromagnetic or ferrimagnetic (FM) layers in contact with antiferromagnetic (AF) layers, and core-shell nanoparticles, with FM core and an AF shell.[2] However, certain AF-AF interfaces are also known to produce exchange bias.[3] Extremely large exchange bias of more than 1 T at 5 K occurs in natural samples with ilmenite-exsolution lamellae in a hematite matrix,[4] carrying uncompensated moments at the interface between bulk AF hematite and AF ilmenite lamellae.[4–6] The ilmenite lamellae are three-dimensional nanometer-scale inclusions in the bulk hematite matrix. They do not form extended planar structures comparable to thin films.[5,7,8] To understand the physical mechanism of exchange bias in this system, we developed a general micromagnetic model describing isolated FM nanoparticles embedded in an AF matrix, which covers lamellar magnetism as a special case. For hematite-ilmenite lamellae this model complements an earlier atomistic Monte-Carlo study of Ref. 9.

For thin films and uniaxial magnetocrystalline anisotropies[2] the total energy $E(\phi_0)$ per surface S, is

$$E/S = 2\sqrt{AK}(1-\cos\phi_0) - M_{\mathrm{FM}}Ht_{\mathrm{FM}}\cos\phi_0 + K_{\mathrm{FM}}t_{\mathrm{FM}}\cos^2\phi_0. \qquad (1)$$

Here, ϕ_0 denotes the deflection angle of the bulk FM moment, and nearby AF spins, from the easy axis. The thickness of the FM layer is t_{FM}, and K_{FM} is the FM anisotropy constant. A denotes the phenomenological exchange constant and K the bulk magnetic anisotropy constant of the AF matrix. The $\cos\phi_0$ term in the total energy implies that inverse magnetization states have different energies. This asymmetry is due to the presence of a domain wall (DW) in the higher-energy reversed state and results in a bias field[2]

$$H_E \approx \sqrt{AK}/(M_{\mathrm{FM}}t_{\mathrm{FM}}), \qquad (2)$$

inversely proportional to t_{FM}. In case of small magnetic inclusions, with particle radius r_0 less than the AF domain-wall width $\sim\lambda_{\mathrm{AF}}=\sqrt{A/K}$, the thin-film approximation is not applicable, and the inclusions must be regarded rather as FM nanodots in the AF matrix.

In Sec. II, we demonstrate by micromagnetic calculation that the AF DW around a deflected FM nanodot approximately contains the energy

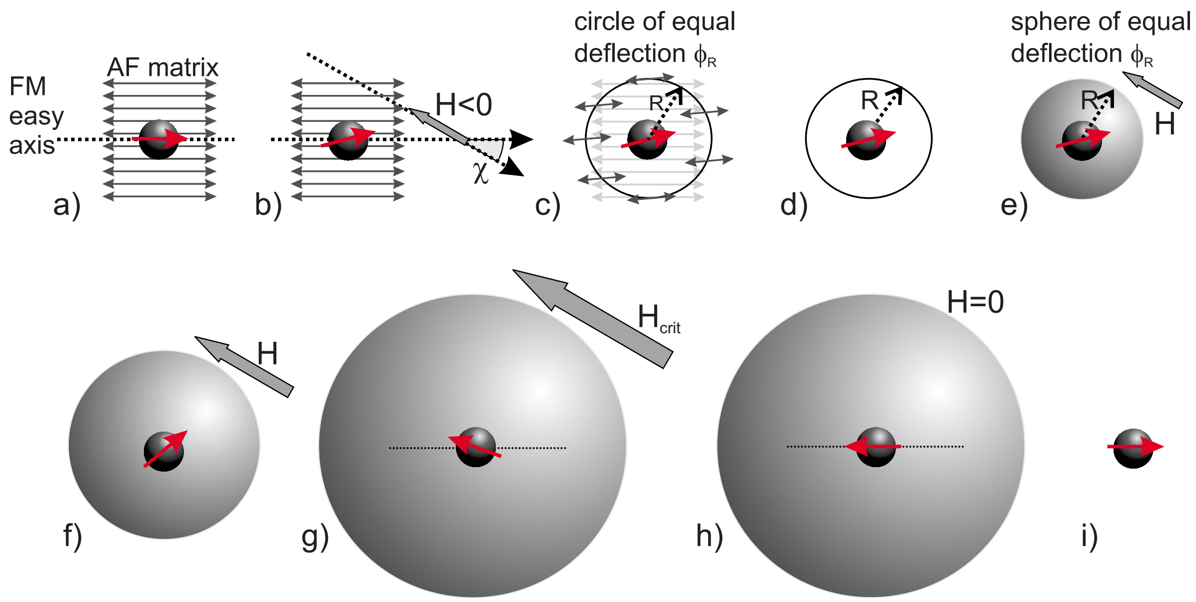

FIG. 1. (Color online) In equilibrium position (a), the FM moment of the nanodot is embedded in the AF matrix and aligned with its easy uniaxial axis which is assumed to be parallel to the AF sublattice magnetization direction. Applying a small negative field H at an acute angel χ in (b) rotates the FM moment, while the AF matrix experiences no magnetic torque. However, the tilted FM moment also deflects the exchange-coupled AF matrix (c). The AF deflection rapidly decays with distance from the nanodot, and one can define a circle of constant deflection ϕ_R (d), whose varying radius R serves as a visual representation of the rotation in the AF matrix. In three-dimensional space, equal deflection actually occurs on concentric spherical shells as drawn in (e). Increasing the negative field strength in (f), increases R. For high anisotropy energies, the moment switches to a more favorable position at some critical field strength $H_{\rm crit}$ (g). Removing the field at this state (h), moves the FM moment toward its inverse easy anisotropy position, which still requires a spherical AF domain wall around the nanodot. This new state (h) has a higher energy than the previous state (i) without the spherical AF wall.

$$E_{\rm DW}=4\pi\sqrt{AK}(r_0\lambda_{\rm AF})\phi_0^2. \qquad (3)$$

Based on this domain-wall energy, we then develop in Sec. III a modified Stoner-Wohlfarth model, to describe all possible hysteresis loops of isolated nanodots by a two-parameter family, depending on scaled anisotropy energy and field direction.

B. Overview of the physical mechanisms

We here briefly sketch the two main physical ideas of our isolated-nanodot model, the structure of the energy term in Eq. (3), and the mechanism of exchange bias. The FM nanodot, embedded in the AF matrix, is approximated by a magnetized sphere with a single, uniaxial easy axis in Fig. 1(a). By applying a field H at some angle, the FM moment rotates into angle ϕ_0 and drags the AF matrix along [Fig. 1(b)]. The locally rotated AF spins create a high exchange-energy density, which must be rapidly relaxed by AF spin rotation from ϕ_0, at the nanodot interface, to almost zero within some distance R, which either has the characteristic dimension $\lambda_{\rm AF}$ of the planar AF DW width or of the sphere radius r_0 [Fig. 1(c)]. The smaller value is physically plausible, because it creates a smaller total exchange energy. This will be shown formally in Sec. II. One then has $R\propto r_0$, and the exchange-energy density is about $A[\nabla\phi(r)]^2\approx A(\phi_0/r_0)^2$, which yields the AF-DW energy in Eq. (3). This DW energy is proportional to the FM-nanodot *diameter* not to its surface area as in case of thin films.

To understand the origin of exchange bias one has to consider minimization of exchange energy plus anisotropy energy within the AF matrix. Substantial matrix deflection, larger than some small angle $\phi_R=\alpha$, occurs within the spherical shell of radius R [e.g., $\alpha=5°$ in Figs. 1(c)–1(e)]. Increasing H, also increases ϕ_0 and thereby R [Fig. 1(f)]. If the anisotropy energy of the nanodot is sufficiently high it creates an energy barrier higher than the energy needed to deflect the matrix. In this case—and only then—there exists a critical field strength, above which the FM moment irreversibly switches to an energetically more favorable position closer to its easy anisotropy axis [Fig. 1(g)]. Removing the field at this state can even leave the nanodot moment close to opposite to its initial direction [Fig. 1(h)]. Unlike the initial state, the new inverse metastable state requires a spherical AF domain wall around the nanodot. Therefore, the new state in Fig. 1(h) has higher energy than the initial state, without a spherical AF DW [Fig. 1(i)]. This energetic asymmetry between oppositely magnetized states shifts the hysteresis loop toward negative fields with respect to the field direction indicated in Fig. 1(b). The growth of the spherical DW surface area in Fig. 1 visually supports the claimed quadratic increase in DW energy with ϕ_0 in Eq. (3). For large ϕ_0 this term is distinctively different from the empirical cos ϕ_0 relation[1,2] for thin films. Estimating the possible bias field H_E by again equating AF-DW energy with the magnetostatic energy, the nanodot bias turns out to be inverse proportional to r_0^2, and thus increases considerably faster with decreasing r_0 than H_E for thin films increases with decreasing $t_{\rm FM}$.

Formally, Eq. (3) resembles an elastic-torque energy for the magnetic moment, where torque increases linearly with deflection. The qualitative reason for this torque is that, other than planar domain walls which have a fixed energy of formation, a spherical DW around a nanoparticle cannot propagate indefinitely through the AF matrix, because its surface and energy increase quadratically with radius. As a cautious note we add that this picture describes only isolated nanodots, where the spacing between nanodots in the AF matrix is large in comparison to nanodot size and λ_{AF}. Collective switching in dense nanodot systems is the topic of ongoing research.

II. AF DOMAIN-WALL ENERGY AROUND AN EMBEDDED MAGNETIC NANOPARTICLE

We consider a homogenous magnetic moment **m**, strongly exchange coupled to the surrounding AF matrix. The moment either originates from a FM inclusion (e.g., in core-shell nanoparticles) or from a surface moment due to uncompensated spins of the AF lattice (e.g., ilmenite lamellae in hematite matrix[5]). In the continuum theoretical description the magnetization orientation of the AF matrix is represented by the antiferromagnetic vector

$$\mathbf{t} = (\mathbf{a} - \mathbf{b})/2 \tag{4}$$

of its antiparallel sublattice moments **a** and **b**, belonging to adjacent AF planes.[3]

A. Micromagnetic energy contributions

In the micromagnetic approximation, the physical state of the system is obtained by minimizing the sum of the following energies. (1) Exchange energy of the antiferromagnetic lattice

$$\int_{V_{\mathrm{AF}}} A(\nabla \mathbf{t})^2 dV, \tag{5}$$

where A is the phenomenological exchange constant of the AF matrix, and the integral is over the volume V_{AF} of the AF matrix.

(2) Anisotropy of the antiferromagnetic lattice

$$\int_{V_{\mathrm{AF}}} K[1 - (\mathbf{t} \cdot \mathbf{u})^2] dV \tag{6}$$

where K is the volume-specific uniaxial anisotropy constant and $\pm\mathbf{u}$ represents the easy axis of the AF matrix.

(3) Magnetocrystalline anisotropy of the embedded moment

$$K_v[1 - (\mathbf{m} \cdot \mathbf{v})^2], \tag{7}$$

where K_v is the uniaxial anisotropy energy of the embedded moment **m** and $\pm\mathbf{v}$ points in the easy axis for **m**.

(4) Anisotropy energy of the interface exchange coupling

$$-D\mathbf{m} \cdot \mathbf{t}, \tag{8}$$

where D is the interface-coupling energy between FM moment and AF matrix. In the following we will assume that this coupling is strong enough, to consider **m** and **t** as being essentially parallel.

(5) External-field energy of the embedded moment

$$-\mu_0 \mathbf{m} \cdot \mathbf{H}, \tag{9}$$

where **H** is the external field vector. In addition, the FM inclusion is assumed to be homogeneously magnetized throughout.

B. Outline of the approximation

To calculate the domain-wall energy around a nanodot we describe the bulk AF matrix outside the particle by its AF vector $\mathbf{t}(\mathbf{r})$.[3] We impose the boundary condition of homogenous nanodot magnetization, which requires a constant value $\mathbf{t}(\mathbf{r}) = \mathbf{t}_0$ on the particle surface. At infinity we request $\mathbf{t}(\mathbf{r}) = \mathbf{u}$. The total energy in the AF matrix is the sum of Eqs. (5) and (6), which in the appropriate units of λ_{AF} for length, and $A\lambda_{\mathrm{AF}}$ for energy, is given by

$$e_{\mathrm{AF}} = \int_{V_{\mathrm{AF}}} [\nabla \mathbf{t}(\mathbf{r})]^2 + \{1 - [\mathbf{t}(\mathbf{r}) \cdot \mathbf{u}]^2\} dV. \tag{10}$$

Minimization of e_{AF} under the boundary conditions then yields the $\mathbf{t}(\mathbf{r})$ dependence for the spherical domain wall. The nonlinear terms in Eq. (10) make an exact analytical solution impossible. Therefore we first derive an approximate analytical solution for spherical and spheroidal particles, which allows for a systematic understanding and classification of the hysteresis processes. The validity of this approximation is subsequently supported by comparison to accurate numerical solutions of the exact equation.

C. Mathematical treatment of exchange energy

In the following, the angle ϕ describes a rotation of **t** in the x-y plane, spanned by the uniaxial easy axis **u** and the field direction. The out-of-plane component is described by θ, such that $\mathbf{t} = (\cos\theta\cos\phi, \cos\theta\sin\phi, \sin\theta)$. According to Ref. 10, the exchange energy in Eq. (5) in polar coordinates then becomes

$$e_x = A[(\nabla\theta)^2 + \cos^2\theta(\nabla\phi)^2]. \tag{11}$$

The Euler-Lagrange equations for only minimizing Eq. (11) under the given boundary conditions are

$$\Delta\theta + \sin 2\theta(\nabla\phi)^2 = 0,$$

$$\cos^2\theta\Delta\phi - \sin 2\theta \nabla\phi \nabla\theta = 0. \tag{12}$$

The choice of $\theta = 0$, $\Delta\phi = 0$ yields a solution of these equations, which has minimal energy, because Eq. (11) is nonnegative. Because $\theta = 0$ also minimizes Eq. (6), minimizing the exchange energy in Eq. (11) for this case simplifies to minimizing

$$e_x = A(\nabla\phi)^2. \tag{13}$$

This ensures that the magnetization always lies in the x-y plane, and only the angle ϕ is relevant in the following.

D. Approximate analytical DW energy

For the approximate analytical solution, we split V_{AF} into an inner region V_1 and an outer region V_2. The boundary between these regions is chosen to coincide with the surface where $\phi=0.5$. Inside V_1, close to the particle surface, the large deviation from the easy anisotropy axis requires that rapid angular variation occurs. Exchange energy dominates the magnetization *change* in V_1, because anisotropy energy itself, although high, is bounded in V_1. Therefore, it can be neglected for the minimization. This seems paradoxical, however, the need to diminish the anisotropy energy in V_1 is taken into account by the boundary conditions, which require the rapid change from the nanodot surface to the outer boundary of V_1. The details of this change are then dominated by the exchange energy, which tries to avoid large gradients. In the outer region V_2 the deflection of ϕ from zero is small, and after linearizing the sin ϕ term, the Euler-Lagrange equation becomes a Helmholtz equation, which can be solved analytically.

After the simplification in Sec. II C, the rescaled total energy in spherical coordinates is

$$E = 4\pi \int_{\epsilon}^{\infty} r^2[\partial_r \phi(r)]^2 + r^2 \sin^2 \phi(r) dr. \tag{14}$$

Neglecting anisotropy energy leaves in V_1 the energy

$$E_1 \approx 4\pi \int_{\epsilon}^{R} r^2[\partial_r \phi(r)]^2 dr. \tag{15}$$

In the outer region V_2, replacing sin ϕ by ϕ yields

$$E_2 \approx 4\pi \int_{R}^{\infty} r^2[\partial_r \phi(r)]^2 + r^2 \phi(r)^2 dr. \tag{16}$$

The cutoff radius R between the two regions depends on the choice of the angular deviation ϕ_R at R and on the nanoparticle radius ϵ. As shown in Sec. II C, minimizing Eq. (15) leads to the Laplace equation

$$r\partial_r^2 \phi(r) + 2\partial_r \phi(r) = 0 \tag{17}$$

for $\phi(r)$ in V_1, which also must fulfill the boundary conditions

$$\phi(\epsilon) = \phi_0, \quad \phi(R) = \phi_R. \tag{18}$$

The unique solution of this boundary value problem is

$$\phi_1(r) = \phi_0 \frac{\epsilon}{r}\frac{R-r}{R-\epsilon} + \phi_R \frac{R}{r}\frac{r-\epsilon}{R-\epsilon}, \tag{19}$$

which gives the energy

$$E_1(\phi_1) = 4\pi\epsilon(\phi_0 - \phi_R)^2 \frac{R}{R-\epsilon}. \tag{20}$$

Minimizing Eq. (16), leads to the Euler-Lagrange equation

$$r\partial_r^2 \phi(r) + 2\partial_r \phi(r) - r\phi(r) = 0 \tag{21}$$

for $\phi(r)$ in V_2, which must fulfill the boundary conditions

$$\phi(R) = \phi_R, \quad \phi(\infty) = 0. \tag{22}$$

This Dirichlet problem has the unique solution

$$\phi_2(r) = \phi_R \frac{R}{r} e^{(R-r)}, \tag{23}$$

with energy

$$E_2(\phi_2) = 4\pi\phi_R^2 R(1+R). \tag{24}$$

The combined approximate solution is obtained by minimizing the total energy $E_1(\phi_1)+E_2(\phi_2)$ with respect to ϕ_R, which yields

$$\phi_R = \phi_0 \frac{\epsilon}{R(1+R-\epsilon)}. \tag{25}$$

This solution also turns out to be differentiable at $r=R$. An appropriate cutoff radius R is found by requesting that $\phi_R = \min(\phi_0, 0.5)$, which is smaller than ϕ_0 and also justifies the linearization in V_2. The resulting expression for R is

$$R = \max\left(\epsilon, \frac{1}{2}[\epsilon - 1 + \sqrt{(\epsilon-1)^2 + 8\epsilon\phi_0}]\right). \tag{26}$$

Thus, the cutoff radius R is of order ϵ. This physically means that the initial deflection ϕ_0 dies out, over a characteristic distance on the order of the inclusion size r_0, instead of over the larger size λ_{AF} as in the thin-film case. The approximative total energy of a spherical nanodot, with radius ϵ and deviation angle ϕ_0, is

$$E(\phi_0, \epsilon) = 4\pi\epsilon^* \phi_0^2, \tag{27}$$

where

$$\epsilon^* = \min\left(\epsilon(1+\epsilon), \epsilon + \frac{\epsilon}{4\phi_0}[\epsilon - 1 + \sqrt{(\epsilon-1)^2 + 8\epsilon\phi_0}]\right) \tag{28}$$

lies always between ϵ and $\epsilon(1+\epsilon)$, and for $\epsilon \ll 1$, in second order approximation, is equal to $\epsilon(1+\epsilon)$ (Fig. 2). This result justifies the qualitative energy term in Eq. (3) in the introduction, and improves it by second-order terms in ϵ and by the additional ϕ_0 dependence. The latter becomes important only for large ϕ_0.

E. Comparison between approximate and exact solution

The approximate solution in Eq. (27) can be tested by numerically solving the Euler-Lagrange equation for Eq. (14). We do this for a spherical nanodot with radius r_0 and for boundary conditions $\phi(r_0)=\phi_0$ and $\phi(\infty)=0$, by using the shooting method for ordinary differential equations on a sufficiently large, but finite interval. The variation in energy as a function of ϕ_0 in comparison to Eq. (27) is shown in Fig. 3 for $\epsilon=0.9$. The inset of Fig. 3 directly compares the radial variation $\phi(r)$ for one approximate solution according to Eqs. (19) and (23) (dashed line) to the exact numerical solution (solid). Even though the difference between solution and approximation is visible, it is not crucial for the qualitative behavior. The corresponding energies deviate by less than 15% for this case.

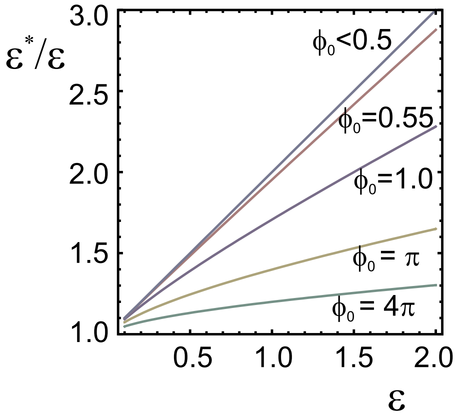

FIG. 2. (Color online) Relation between real nanodot radius ϵ and its effective radius ϵ^* defined in Eq. (27). Using Eq. (28), the graph plots the relation ϵ^*/ϵ for different values of ϵ and ϕ_0. For small $\phi_0 \leq 0.5$ the effective size is $\epsilon^* = \epsilon(1+\epsilon)$, while for large ϕ_0, ϵ, and ϵ^*/ϵ approaches 1. ϵ always underestimates ϵ^*, but at most by the factor $1+\epsilon$.

F. Extension to oblate ellipsoidal nanodots

The energy expression (27), derived for spherical nanodots, can be generalized analytically to a nanodot, which is an ellipsoid of revolution with scaled minor axis $\epsilon_{\min}$ directed along the z axis, and two major axes $\epsilon_{\max}$ in the (x,y) plane. For an external field applied in the (x,y) plane, the deflected magnetic moment is $m = [\cos(\phi_0), \sin(\phi_0), 0]$. The spatial variations in the AF vector **t** outside the nanodot are again described by ϕ, but now in oblate spheroidal coordinates (σ,τ) as defined in Ref. 11. For the possible range of $\sigma \geq 0$, $-1 \leq \tau \leq 1$, the surfaces of constant σ are oblate spheroids. Their focal distance a is chosen such that a surface $\sigma = \sigma_0$ coincides with the particle surface when $\epsilon_{\max} = a\sqrt{1+\sigma_0^2}$ and $\epsilon_{\min} = a\sigma_0$. Thereby, the boundary conditions are

$$\phi(\sigma_0) = \phi_0, \quad \phi(\infty) = 0. \tag{29}$$

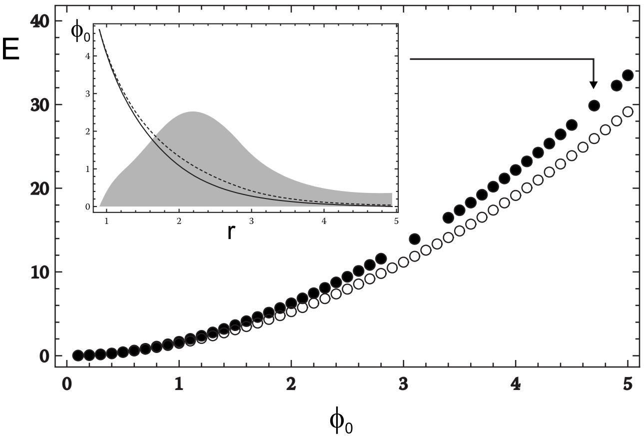

FIG. 3. Comparison between energies of exact numerical solution (filled dots) and approximation (circles) for $\epsilon = 0.9$ as a function of ϕ_0. The inset shows the radial dependence of the solution $\phi(r)$ for $\phi_0 = 4.7$. The shaded area is the 10× magnified difference between exact solution (solid line) and approximation (dashed).

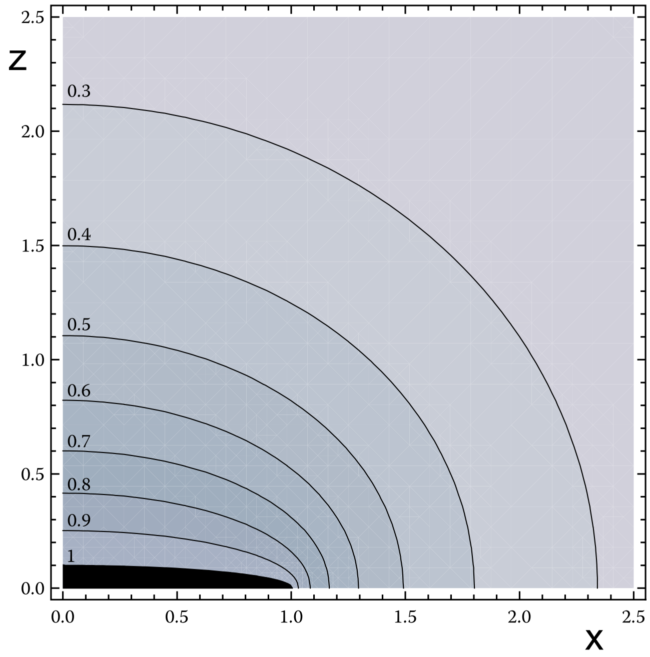

FIG. 4. (Color online) Variation in ϕ around an oblate elliptical nanodot (black). Units are scaled to λ_{AF}, and contour labels indicate rotation angles in multiples of π. The diagram shows only one quarter of the cross-section. The z axis is the rotation axis.

Minimizing the exchange energy in Eq. (13) corresponds to solving the Laplace Eq. (12) for $\theta = 0$, and yields

$$\frac{\partial}{\partial\sigma}\left[(1+\sigma^2)\frac{\partial\phi}{\partial\sigma}\right] = 0. \tag{30}$$

The complete boundary value problem has the solution

$$\phi(\sigma) = \frac{\arctan(1/\sigma)}{\arctan(1/\sigma_0)}\phi_0, \tag{31}$$

which neglects anisotropy energy, but results in a good, lower estimate of the total energy

$$E \gtrapprox E_{\text{ex}} = \frac{4\pi a^3\phi_0^2}{\arctan^2(1/\sigma_0)}\int_{\sigma_0}^{\infty}\int_0^1 \frac{d\tau d\sigma}{a^2(1+\sigma^2)} = \frac{4\pi a\phi_0^2}{\arctan(1/\sigma_0)}. \tag{32}$$

This expression demonstrates that the AF domain-wall energy around an oblate nanoparticle also depends quadratically on ϕ_0. In the spherical limit $\sigma_0 \to \infty$ while keeping $\epsilon_{\min} = a\sigma_0$, Eq. (32) becomes $4\pi\epsilon_{\min}\phi_0^2$, which is exactly the expression for the sphere. The limit of a very flat spheroid corresponds to $\sigma_0 \ll 1$, and Eq. (32) becomes $E \approx 8\epsilon_{\max}\phi_0^2$. This is the same energy as for a sphere with radius $\epsilon = 2/\pi\epsilon_{\max}$, despite the drastic difference in volume. The result indicates that the energy expression (27), derived for a spherically shaped nanodots, essentially describes any flat object of approximately the same characteristic radius. The angular variation, inferred from calculated ϕ—contours in the vicinity of an oblate ellipsoid (Fig. 4), is most rapid in regions of small elliptical dimension, where integrating over a high exchange-energy *density* does not lead to a high *total energy*. Thereby, the surfaces of equal ϕ rapidly become more spherical.

III. HYSTERESIS OF NANODOTS

A. Energy contributions

In the previous section we have shown that the AF domain-wall energy for isolated spherical nanodots in good approximation is given by Eq. (27). Calculating the hysteresis loops of spherical nanodots requires two additional energy terms. First, the external field energy

$$E_{ext}(\phi,r_0) = -4\pi\mu_0 H\left(\mu r_0^2 + \frac{M_s}{3}r_0^3\right)\cos(\phi-\chi), \tag{33}$$

where the field H is applied in the basal plane with angle χ versus the easy axis of the AF matrix, and the particle moment is assumed to change proportional to the sphere's surface as $4\pi\mu r_0^2$, where μ is the specific surface moment of the particle. A bulk FM moment is taken into account through the term $4\pi M_s/3r_0^3$. In addition, there is the anisotropy energy E_{an}, which describes a preferred magnetization axis of either the surface moment or the bulk FM moment. The surface part of this anisotropy again scales with $4\pi r_0^2$, while the anisotropy of the inner volume scales with $4\pi/3r_0^3$. Thus we obtain

$$E_{an}(\phi,\epsilon) = -4\pi K_s r_0^2\cos^2(\phi-\alpha_s) - \frac{4\pi}{3}K_v r_0^3\cos^2(\phi-\alpha_v), \tag{34}$$

where α_s and α_v determine the easy directions, and K_s and K_v are the anisotropy constants of surface and volume anisotropy, respectively. The two simplest cases are (1) to consider only surface anisotropy, surface moments, and assume $\alpha_s=0$ or (2) to consider only volume anisotropy, volume magnetization and $\alpha_v=0$. Using ϵ^* from the previous section, the scaled total energy in the first case is

$$e_s = \frac{1}{4\pi A\sqrt{A/K}}E_s = \epsilon^*\phi^2 - h\epsilon^2\cos(\phi-\chi) - \kappa_s\epsilon^2\cos^2\phi, \tag{35}$$

where h is measured in units of $\sqrt{AK}/(\mu_0\mu)$, and κ_s in units of $\sqrt{AK}$. In the second case one obtains

$$e_v = \frac{1}{4\pi A\sqrt{A/K}}E_v = \epsilon^*\phi^2 - \frac{1}{3}h\epsilon^3\cos(\phi-\chi) - \frac{1}{3}\kappa_v\epsilon^3\cos^2\phi, \tag{36}$$

where now h is $\mu_0 M_s H/K$ and κ_v is K_v/K.

B. A Stoner-Wohlfarth model of embedded nanodot hysteresis

To obtain a simplified description of the general hysteresis properties of isolated nanodots embedded in an AF matrix, it is assumed that ϵ^* in Eq. (27) is a constant effective diameter of the nanodot. This approximation simplifies the above more complete physical theory to a model system, which is described by the energy function

$$e^* = \phi^2 - h^*\cos(\phi-\chi) - k^*\cos^2\phi. \tag{37}$$

Here h^* represents the field and k^* the anisotropy constant. Both are additionally scaled by particle size ϵ^*. In the case of surface energies as in Eq. (35), k^* corresponds to $\kappa_s\epsilon^2/\epsilon^*$ and h^* to $h\epsilon^2/\epsilon^*$. For volume energies as in Eq. (36), $k^*=1/3\kappa_v\epsilon^3/\epsilon^*$ and $h^*=1/3h\epsilon^3/\epsilon^*$. The only real simplification in this model system is the neglect of the ϕ dependence of the coefficient ϵ^* of ϕ^2 in Eq. (27). The hysteresis loops, obtained by minimizing Eq. (37), form a two-parameter family and are easily characterized. The minima of Eq. (37) are defined by

$$\frac{\partial e^*}{\partial\phi} = 2\phi + h^*\sin(\phi-\chi) + k^*\sin(2\phi) = 0, \tag{38}$$

$$\frac{\partial^2 e^*}{\partial\phi^2} = 2 + h^*\cos(\phi-\chi) + 2k^*\cos(2\phi) > 0. \tag{39}$$

The switching field is found by setting both derivatives to zero in Eqs. (38) and (39). In a uniaxial field, for given k^*, χ, and h^*, the energy can be plotted as a function of ϕ. By starting in the unique global-energy minimum at large positive field h^*, one can stepwise change the field and trace the evolution of the minimum state. In this way a hysteresis loop can be calculated for each pair of values for k^* and χ. The resulting two-parameter family of hysteresis loops is represented in the phase diagram in Fig. 5. Three main regions can be distinguished. First a region of low k^*, or large χ, where all magnetization changes are reversible due to the dominance of the ϕ^2 domain-wall energy term [Fig. 5(C)]. The second region has intermediate k^* and contains negatively shifted loops with irreversible switching processes [Figs. 5(A) and 5(B)], corresponding to 180° spherical domain walls pinned by anisotropy energy as sketched in Figs. 1(g) and 1(h). In the third region domain walls with larger rotation angles occur [Fig. 5(D)].

A typical shifted loop due to 180° domain-wall formation is shown in Fig. 6. Here, at the positive field $h^*=5$ a clear single minimum state with positive $\phi_{\min}$ exists [Fig. 6(b)]. For larger fields, additional metastable minima appear, which correspond to $\approx\pm 2\pi$ rotated states with additional 360° AF spherical domain walls. When the field is decreased to −9 the moment is caught by the negative anisotropy direction which stabilizes the spherical domain wall. At large negative fields, two separate minima exist. They correspond to two possible domain walls for rotation angles of the moment lying $\approx 2\pi$ apart. Reducing the field, switches the angle back to values close to $\phi=0$ only at about $h^*=-5$ [Fig. 6(b)].

A more complicated process occurs in the upper region of the phase diagram [Fig. 5(D)]. A typical loop in this region starts with positive ϕ for state A in a large positive field $h^*=20$ in Fig. 7, where the moment tries to align with the field. By reducing the field, the moment rotates backward until at some negative field value in state B it switches into negative alignment with its easy axis [B → C in Fig. 7(b)], because the gain in anisotropy energy by switching to state C is larger

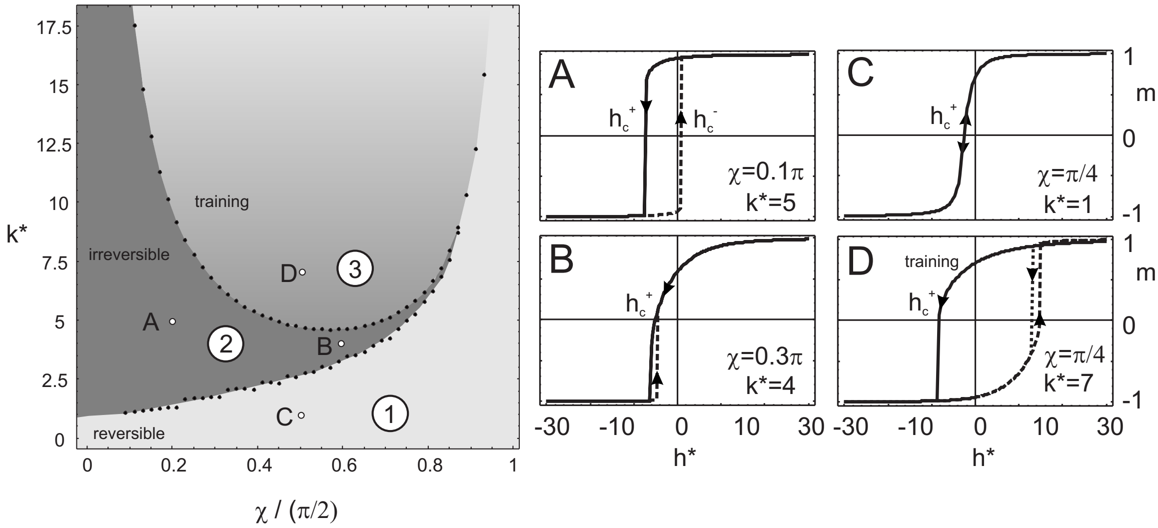

FIG. 5. Phase diagram of nanodot hysteresis properties. The three regions delineate (1) reversible negatively biased loops for small k^* (c), (2) biased irreversible loops with hysteresis and 180° AF domain walls (A,B), (3) reversible or irreversible positively biased loops which after the first "training branch" form 360° AF domain walls (d). At even higher k^* further subdivisions of region 3 exist, which are not delineated here. They correspond to formation of $n\times 180°$ walls with $n>2$ and are probably of little practical importance. The right panel shows four characteristic examples of loops in the three regions. They are calculated by starting at $h=30$ and decreasing the field to $h=-30$ (solid line), then the field is again increased to $h=30$ (dashed) and decreased to $h=-30$ (dotted). In C all three curves are the same, in A and B the dotted line falls on the solid line.

than the increase in DW energy. Because the anisotropy of $k^*=5.5$ is strong enough, the moment in state C is more than 180° away from the positive-field direction χ. Therefore, the moment will never rotate back from $\mathrm{C}\rightarrow\mathrm{B}$ by increasing the field. Instead, it will continue to rotate toward more negative angles, in spite of increasing DW energy. At some point it even switches again into positive alignment with its easy anisotropy axis [$\mathrm{C}\rightarrow\mathrm{D}$ in Fig. 7(b)]. Because subsequent field cycling never restores the initial lowest-energy state, the first hysteresis branch $\mathrm{A}\rightarrow\mathrm{B}$ is a "training" branch for the final loop between a state with a 180° and a 360° wall. For even larger k^*, this training process can theoretically be repeated several times until the final loop switches between a state with a $(n-1)\times 180°$ DW and one with a $n\times 180°$ DW.

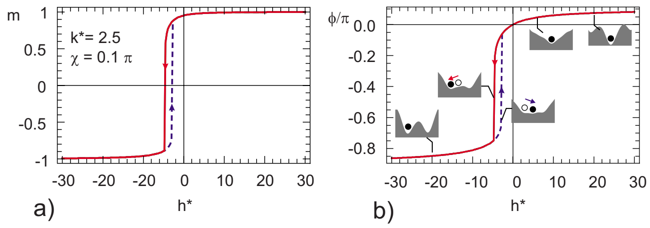

a) b)

FIG. 6. (Color online) Modeled hysteresis loop for $k^*=2.5$, $\chi=0.2(\pi/2)$ for h^* between −30 and 30. The magnetic moment (a) is clearly shifted due to domain-wall formation. The hysteresis of the FM angle ϕ (b) shows the asymmetric switching between the energy minima. The insets in (b) depict energy as a function of ϕ and show which magnetization state is assumed (black dots). The insets also indicate why the irreversible switching processes occur only at negative h^* (circle to dot).

IV. DISCUSSION AND CONCLUSIONS

A. Modeling natural ilmenite lamellae in a hematite host

The initial aim of this study was to explain the unusual low-temperature hysteresis properties measured on natural samples from an area of a negative magnetic anomaly over

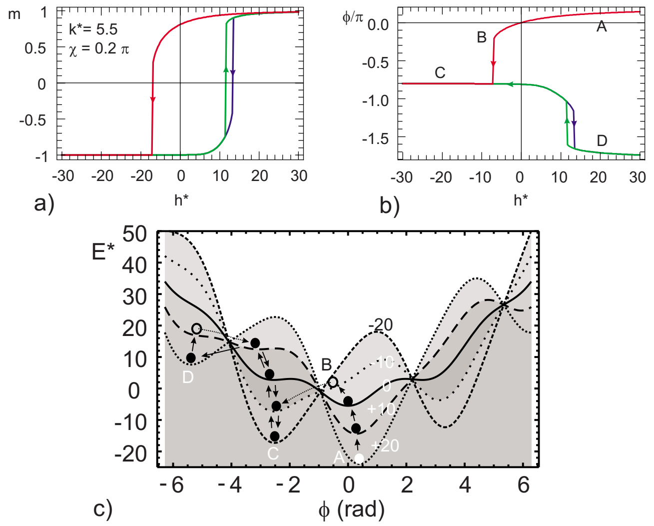

a) b) c)

FIG. 7. (Color online) Energy plots for $k^*=5.5$, $\chi=0.4(\pi/2)$, and different values of $h^*=20,10,0,-10,-20$. The minimum state is indicated by a disk. Starting at $h^*=20$ in state A, the field is decreased until in state B the minimum becomes unstable and irreversibly shifts to smaller ϕ in state C. All further variations in h^* between −20 and 20 shift the minimum state between C and D. The initial state A cannot be reached.

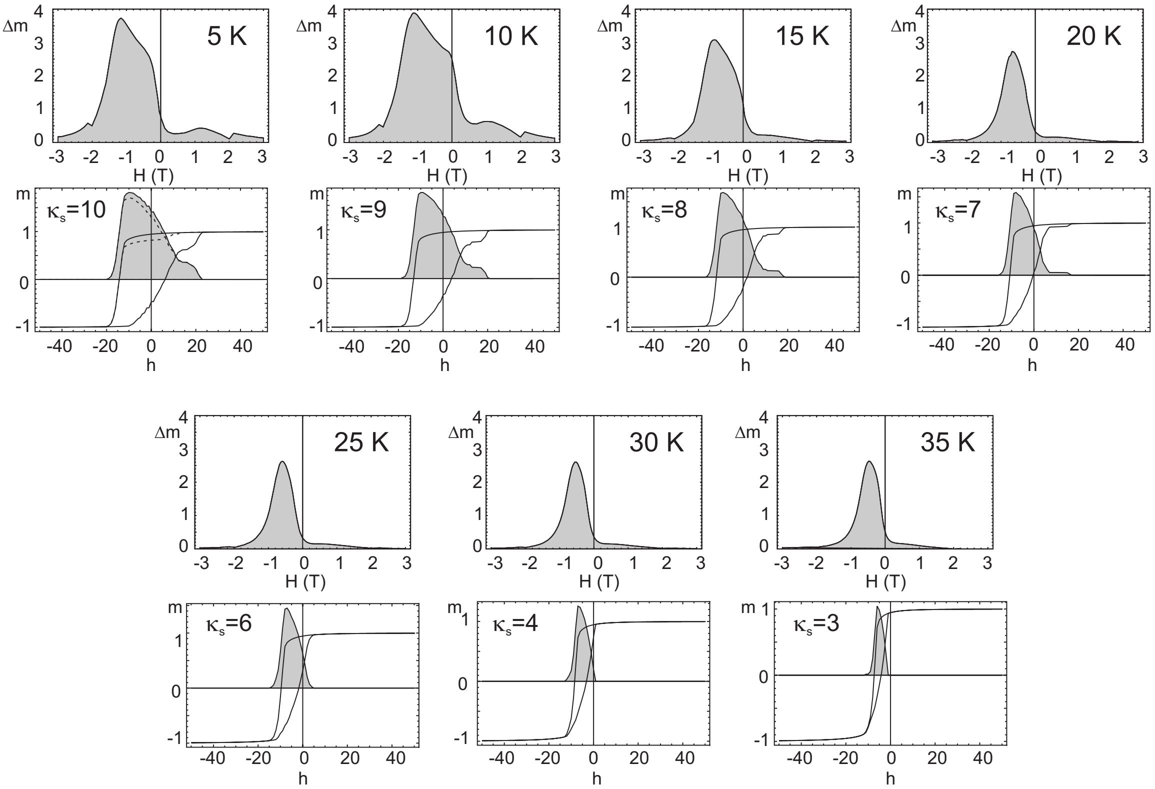

FIG. 8. The first and third rows show a sequence of hysteresis differences, measured at increasing T for sample MODLB-2 after imposing a 7 T field at room temperature, and cooling in zero field to 5 K. The exchange bias during warming vanishes close to ilmenite's Néel temperature of 57 K. Shape and size of the biased loops may contain information about the spectrum of lamella size and magnetic moment. The even rows show modeled hysteresis differences for an ensemble of nanodots according to Eq. (35) with $\epsilon^* = \epsilon$, which has a fixed distribution of lamella sizes $\epsilon = 0.3 - 1$ in steps of 0.05, and an angular average from $\chi = 0.1\pi/2 - 0.3\pi/2$ in steps of $0.05\pi/2$. The distribution function is chosen proportional to $1/\epsilon^2$, such that all modeled curves contribute equally to the moment. By varying the surface anisotropy of the nanodot from $\kappa_s = 10$ down to $\kappa_s = 3$, the obtained hysteresis differences resemble the measured curves.

the 1 Gyr-old metamorphic complex in the Modum district, South Norway. These exsolved rhombohedral oxides of hematite with ilmenite exsolution have astonishing magnetic properties, related to unbalanced magnetic moments at nanoscale exsolution interfaces.[5,8,12–14] The most spectacular observation is low-temperature exchange bias of more than 1 T.[4] During zero-field cooling of the NRM, the onset of ilmenite's AF ordering at $T_N \approx 57$ K induces a remanence drop of about 10%. This implies that the ilmenite phase is magnetically coupled to the NRM carriers, and that this coupling is inverse. The coupling effects are nearly completely reversible upon reheating the sample to room temperature. Curie temperatures of the hematite host are between 610 and 620 °C.[6] Because the lamellar moments arise from uncompensated AF sublattice spins of the hematite host at the interface to ilmenite, these spins are thermally stable almost up to the above Curie temperature. Therefore, at low temperatures, thermal activation of the nanodots can be neglected, apart from the variation in the phenomenological material parameters as functions of T.

In Fig. 8 the results of low-temperature hysteresis measurements from sample MODLB-2 are compared to a selected model calculation. The data shown are the hysteresis difference, the difference between upper and lower hysteresis branches, for the natural sample MODLB-2. The results closely resemble similar measurements on sample MODK-4 in Fig. 6 of Ref. 6. Here, the sample was given a remanent magnetization in an inducing field of +7 T at room temperature and then was zero field cooled to 5 K, followed by a sequence of hysteresis curves between +7 and −7 T, at increasing temperatures. All measurements were performed in a MPMS-XL (Quantum Design) at the University of Bremen, Germany.

The first and third rows in Fig. 8 display the measured hysteresis differences, which only represent the irreversible magnetization processes, thereby canceling all reversible signals from admixed paramagnetic minerals in the natural sample. To compare these data with model results, it is assumed that the lamellae have pure surface moments from uncompensated spins at the AF-AF interfaces, and that their surface anisotropy $\kappa_s(T)$ is related to ilmenite, and increases with decreasing temperature below $T_N = 57$ K. In the natural samples, the lamellae share a coherent interface with the hematite host, such that the field direction should not be spherically averaged, as for isotropic samples. It is found, that using Eq. (35) with $\epsilon^* = \epsilon$, and a fixed lamella size distribution from $\epsilon = 0.3 - 1$, the experimentally observed change in shape of the hysteresis difference with increasing temperature is qualitatively well reflected by decreasing κ_s from 10 to 3 in the modeled nanodot distribution with field angles

$\chi = (0.1-0.3)\pi/2$. The model results are displayed in the second and fourth rows of Fig. 8. Although this qualitative agreement provides no proof for the correctness of the chosen model, it shows that the proposed mechanism of nanodot hysteresis is able to provide a possible explanation, even for details of the observed hysteresis properties. Especially, the model result that increasing κ_s shifts the negative coercive field H_c^+ of the upper branch to the left, and increases the hysteresis width, i.e., increases H_c^- of the lower branch, seems to coincide with the experimental observation. Therefore, the general structure of the energy Eq. (37) apparently captures the essential features of real hysteresis behavior of embedded nanodots, although, according to microscopic observations, the shapes of natural ilmenite lamellae closer resemble oblate ellipsoids than spheres.[15] However, due to the similarity of the AF DW energies [Eqs. (32) and (27)], the phenomenology of the hysteresis loops remains unchanged for oblate nanodots. Only the parameters h^* and k^* in Eq. (37) have to be properly rescaled. To account for the smaller volume of the oblate ellipsoids, they must be multiplied by $\epsilon_{\text{min}}/\epsilon_{\text{max}}$, whereby both coercive force and bias field increase substantially with flattening. This increase may explain why especially huge exchange bias is observed in natural samples with extremely thin exsolution lamellae of 1–2 nm or less in thickness. The complex nature of lamellar magnetism makes it likely that the competing energy terms in Eq. (37) will have a different physical meaning, or must be extended, in a more advanced theory. Especially the interaction between close-spaced lamellae will lead to collective switching phenomena which needs further study.

B. Scaling of coercivity and exchange bias with particle size

An overall estimate of coercivity H_c is obtained by equating field energy and anisotropy energy in Eq. (37). With $h^* \approx k^*$ this yields $H_c \approx K_v/(\mu_0 M_s)$ for volume moments and $H_c \approx K_s/(\mu_0 \mu)$ for interface moments. Thus, smaller nanodot moments lead to higher coercivity. Note that, due to exchange coupling between nanodot and matrix, this trend is not counteracted by thermal activation.

Unlike for thin films, the nanodot model in Fig. 5 predicts that only reversible loops occur for $k^* < 0.7$. For small ϕ the anisotropy energy varies like $k^*\phi^2$, and therefore k^* must be on the order of 1 to generate an energy barrier, which overcomes the ϕ^2 term of DW energy.

The hysteresis shift due to domain-wall formation for a reversible curve is best estimated by considering that the coercivity of the upper branch H_c^+ is defined by the condition that at this point the magnetic moment is rotated $\pi/2$ away from the field direction χ. Thus $\phi = \chi - \pi/2$, and by inserting this into the minimum condition in Eq. (38) one obtains

$$h_c^+ = -\pi + 2\chi - k^* \sin(2\chi). \qquad (40)$$

For small $k^* \ll 1$ the hysteresis loop is reversible and h_c^+ corresponds to the exchange-bias field, which lies between $-\pi$ and 0. In case of volume moments $h^* = h\epsilon^2/3$, this corresponds to

$$H_E \approx \frac{-3\pi K}{\mu_0 M_s \epsilon^2} = \frac{-3\pi A}{\mu_0 M_s r_0^2}. \qquad (41)$$

For larger k^* in region 2 of the phase diagram, the exchange bias is between h_c^+ and h_c^-. It therefore depends on the width of the hysteresis loop which increases with increasing k^*. Close to the lower phase boundary in Fig. 5, the bias field is substantially greater than the coercive force, and also is sufficiently well estimated by Eq. (41). For large k^* the bias decreases, and even becomes positive for the stable hysteresis curves (after training) in region 3 of the phase diagram. For oblate nanodots with interface moments H_E, unlike H_c, increases by an additional factor $\epsilon_{\text{max}}/\epsilon_{\text{min}}$, leading to even larger bias.

Because the exchange bias according to Eq. (41) is proportional to $1/\epsilon^2$, it grows much faster with decreasing particle size than in the thin-film case, where $H_E \propto 1/t_{\text{FM}}$. This qualitative difference is caused by the decrease in domain-wall energy proportional to nanodot radius ϵ and not proportional to nanodot surface $\propto \epsilon^2$. To emphasize this result, we compare the characteristic bias fields of a nanoparticle ($H_{E,\text{dot}}$) to $H_{E,\text{film}}$ of a thin film[16] with the same thickness $t_{\text{FM}} = \epsilon \lambda_{\text{AF}}$ which yields

$$H_{E,\text{dot}}/H_{E,\text{film}} \approx \frac{3\pi}{2\epsilon}. \qquad (42)$$

Thus, a system of nanodots with size $\epsilon < 1$ can show a considerably stronger bias than a system of thin films with the same thickness.

The proposed nanodot model predicts a training effect of biased hysteresis curves in case of sufficiently high anisotropy k^* and for intermediate field directions as delineated in Fig. 5. The training results from the combination of the quasielastic DW energy and the sinusoidal anisotropy term in Eq. (37), which together can create several energy minima even for large field values (Fig. 7). An initial equilibrium state can then be irreversibly switched to a loop between metastable states.

C. Conclusions

To understand the origin of extremely large exchange bias in natural samples with fine-scale exsolution structures, we here developed the micromagnetic basis for a modified Stoner-Wohlfarth hysteresis model for isolated FM nanodots, exchange coupled to an AF matrix. The essential hysteresis behavior of such nanodots, is qualitatively represented by a two-parameter family of loops, depending on a scaled anisotropy k^* and an acute angle χ between field direction and easy anisotropy axis. It is found that isolated FM nanodots necessarily produce large hysteresis shift if their size is small with respect to the DW width of the matrix. Depending on k^* and χ, also the hysteresis difference can show significant exchange bias (Fig. 5). The modified Stoner-Wohlfarth model predicts training branches for some nanodot hysteresis loops. The training effect is physically explained by formation of AF domain walls with multiple rotations $n \times 180°$, $n = 2, 3, \ldots$. The parameter range where training branches exist is outlined in Fig. 5. For a natural sample of latticeoriented nanoscale ilmenite exsolution lamellae in a hematite matrix, the temperature variation in measured hysteresis differences closely resembles model results for an ensemble of nanodots with surface moments, surface anisotropy, and a narrow range of field angles. The formation of spherical AF domain walls therefore provides a plausible explanation for the extremely large exchange bias observed in this sample. The previous study of Ref. 9 considered a different mechanism based on the local exchange coupling across the hematite-ilmenite contact layer. Their approach is complementary to our results, because it considers the atomistic basis of the interface exchange-coupling energy Eq. (8) and explores the possibility that this coupling is weak with respect to anisotropy energy. Due to model-size restrictions,[9] cannot account for DW-scale rotation in the AF matrix. In contrast, our micromagnetic model focuses on these effects by assuming that exchange coupling is strong across the interface, such that the FM nanodot moment directly rotates the adjacent AF sublattice magnetization.

ACKNOWLEDGMENTS

We wish to thank P. Robinson for valuable discussions. Three anonymous reviewers provided thoughtful comments, which helped to considerably improve the manuscript. We thank T. Frederichs for support during the MPMS measurements performed at the University of Bremen, Germany. We gratefully acknowledge funding through the Norwegian Research Council (MATERA, Nanomat), ESF travel grants to KF and SM through the European Mineral Science Initiative of the EUROCORES program, and NSF funding to Institute for Rock Magnetism, University of Minnesota.

---

*karl.fabian@ngu.no

[1] W. H. Meiklejohn and C. P. Bean, Phys. Rev. **105**, 904 (1957).

[2] J. Nogués, J. Sort, V. Skumryev, S. Suriñach, J. S. Muñoz, and M. D. Baró, Phys. Rep. **422**, 65 (2005).

[3] R. L. Stamps, J. Phys. D **33**, R247 (2000).

[4] S. A. McEnroe, B. Carter-Stiglitz, R. J. Harrison, P. Robinson, K. Fabian, and C. McCammon, Nat. Nanotechnol. **2**, 631 (2007).

[5] P. Robinson, R. J. Harrison, S. A. McEnroe, and R. B. Hargraves, Nature (London) **418**, 517 (2002).

[6] K. Fabian, S. A. McEnroe, P. Robinson, and V. P. Shcherbakov, Earth Planet. Sci. Lett. **268**, 339 (2008).

[7] T. Kasama, U. Golla-Schindler, and A. Putnis, Am. Mineral. **88**, 1190 (2003).

[8] T. Kasama, S. McEnroe, N. Ozaki, T. Kogure, and A. Putnis, Earth Planet. Sci. Lett. **224**, 461 (2004).

[9] R. J. Harrison, S. A. McEnroe, P. Robinson, B. Carter-Stiglitz, E. J. Palin, and T. Kasama, Phys. Rev. B **76**, 174436 (2007).

[10] A. Hubert and R. Schäfer, *Magnetic Domains* (Springer, Berlin, Heidelberg, New York, 1998).

[11] G. A. Korn and T. M. Korn, *Mathematical Handbook for Scientist and Engineers* (McGraw-Hill, New York, Toronto, London, 1961).

[12] S. A. McEnroe, R. Harrison, P. Robinson, U. Golla, and M. J. Jercinovic, J. Geophys. Res. **106**, 30523 (2001).

[13] S. A. McEnroe, R. J. Harrison, P. Robinson, and F. Langenhorst, Geophys. J. Int. **151**, 890 (2002).

[14] P. Robinson, R. J. Harrison, S. A. McEnroe, and R. B. Hargraves, Am. Mineral. **89**, 725 (2004).

[15] T. Kasama, R. E. Dunin-Borkowski, T. Asaka, R. J. Harrison, R. K. Chong, S. A. McEnroe, E. T. Simpson, Y. Matsui, and A. Putnis, Am. Mineral. **94**, 262 (2009).

[16] D. Mauri, H. C. Siegmann, P. S. Bagus, and E. Kay, J. Appl. Phys. **62**, 3047 (1987).